Characterisation of the transmissivity field of a fractured and karstic aquifer, Southern France

Xiaoguang Wang[1*], Abderrahim Jardani[2], Hervé Jourde[3], Lidia Lonergan[1], John Cosgrove[1], Olivier Gosselin[1&4], and Gérard Massonnat[4]

[1]Department of Earth Science and Engineering, Imperial College London, Exhibition Road, London SW7 2AZ, UK

[2]CNRS UMR 6143, M2C, Morphodynamique Continentale et Cotiere, Université de Rouen, Mont-Saint-Aignan, France

[3]Laboratoire Hydrosciences, UMR 5569 CNRS-IRD-UM1-UM2, Université Montpellier 2, 34095 Montpellier, France

[4]Total SA, Avenue Larribau, 64018, Pau Cedex, France

[*]Corresponding author: x.wang12@imperial.ac.uk

E-mails:

Xiaoguang Wang: x.wang12@imperial.ac.uk; Abderrahim Jardani: abderrahim.jardani@univ-rouen.fr; Hervé Jourde: hjourde@univ-montp2.fr; Lidia Lonergan: l.lonergan@imperial.ac.uk; John Cosgrove: j.cosgrove@imperial.ac.uk; Olivier Gosselin: o.gosselin@imperial.ac.uk; Gérard Massonnat: gerard.massonnat@total.com

Abstract

Geological and hydrological data collected at the Terrieu experimental site north of Montpellier, in a confined carbonate aquifer indicates that both fracture clusters and a major bedding plane form the main flow paths of this highly heterogeneous karst aquifer. However, characterising the geometry and spatial location of the main flow channels and estimating their flow properties remain difficult. These challenges can be addressed by solving an inverse problem using the available hydraulic head data recorded during a set of interference pumping tests.

We first constructed a 2D equivalent porous medium model to represent the test site domain and then employed regular zoning parameterisation, on which the inverse modelling was performed. Because we aim to resolve the fine-scale characteristics of the transmissivity field, the problem undertaken is essentially a large-scale inverse model, i.e. the dimension of the unknown parameters is high. In order to deal with the high computational demands in such a large-scale inverse problem, a gradient-based, non-linear algorithm (SNOPT) was used to estimate the transmissivity field on the experimental site scale through the inversion of steady-state, hydraulic head measurements recorded at 22 boreholes during eight sequential cross-hole pumping tests. We used the data from outcrops, borehole fracture measurements and interpretations of inter-well connectivities from interference test responses as initial models to trigger the inversion. Constraints for hydraulic conductivities, based on analytical interpretations of pumping tests, were also added to the inversion models. In addition, the efficiency of the adopted inverse algorithm enables us to increase dramatically the number of unknown parameters to investigate the influence of elementary discretisation on the reconstruction of the transmissivity fields in both synthetic and field studies.

By following the above approach, transmissivity fields that produce similar hydrodynamic behaviours to the real head measurements were obtained. The inverted transmissivity fields show complex, spatial heterogeneities with highly conductive channels embedded in a low transmissivity matrix region. The spatial trend of the main flow channels is in a good agreement with that of the main fracture sets mapped on outcrops in the vicinity of the Terrieu site suggesting that the hydraulic anisotropy is consistent with the structural anisotropy. These results from the inverse modelling

52 enable the main flow paths to be located and their hydrodynamic properties to be
53 estimated.
54

1. Introduction

Fractured and karstified limestone aquifers contain an important proportion of the world's freshwater resources. These aquifers are known to be highly heterogeneous as the main flow paths corresponds to various flow features, such as matrix, fracture and karst, with distinct hydraulic properties (White, 2002). Contrasts in hydraulic transmissivity between these flow components can be up to 5~10 orders of magnitude (Younger, 1993; Kuniansky et al., 2012). Secondly, the spatial distribution and organisation of the flow features within the volume of a fractured/karstified limestone aquifer are commonly complex which leads to significant flow anisotropy in the system. Furthermore, due to the strong spatial variability of flow properties, fractured/karstified limestone aquifers often exhibit complex, multi-scale flow behaviours (Adler and Thovert, 1999; Berkowitz, 2002; Neuman, 2005).

In order to quantitatively characterise groundwater flow in fractured/karstified rocks, hydrogeological models are often constructed to model the flow processes. These models broadly fall into two major categories: the discrete fracture network model (DFN) and the equivalent porous medium model (EPM). The DFN approach is the most appropriate for modelling groundwater flow in fractured, tight rocks where the preferential flow path consists of a few intersecting fractures. In these models, discrete fractures (Long et al., 1982; Dershowitz and Einstein, 1988; Matthai and Belayneh, 2004) or pipes (Jourde et al., 2002a) are treated as the basic component for both representing the fractured medium and flow computation. One of the most appealing features of these models is that the connectivity of flow paths is explicitly expressed. In addition, fracture data gathered from outcrops (distributions of fracture length, spacing, orientation, aperture) can be integrated into the model by generating

81 statistical models for the fracture network. However, the parameterisation and
82 calibration of discrete fracture network models are often challenging as field data
83 describing the location, geometry, spatial distribution and hydraulic properties of each
84 individual fracture and karst feature are often limited. In contrast, the equivalent
85 porous medium models do not explicitly account for the preferential flow paths but
86 they are straightforward and relatively easier to implement and
87 parameterise. Although the EPM models may seem to be oversimplified and
88 less appropriate to conceptually represent fractured rocks, they can still capture the
89 spatial variability of flow properties and the connectivity of preferential flow paths
90 (Gomez-Hernandez et al., 1997; Neuman, 2005). In fact, because of their simplicity in
91 having no pre-assumption about the location and geometry of the fractures, they can
92 be employed and coupled with inversion algorithms to optimise the spatial geometry,
93 connectivity and production properties of the flow paths in fractured systems (Illman,
94 2014).

95 In hydrogeology, pumping tests provide an important data source for aquifer
96 characterisation. The traditional use of the pumping test technique is restricted to a
97 single pumping well and is used to derive averaged hydraulic parameters
98 corresponding to a large region between the pumping and observation wells (Theis,
99 1935; Cooper and Jacob, 1946; Gringarten 1984; Butler and Liu, 1993). Recently,
100 hydraulic tomography techniques have been applied to reconstruct the spatial
101 variability of the hydraulic properties of aquifers (Neuman, 1987; Butler et al., 1999).
102 Hydraulic tomography is based on a joint analysis of multiple sets of hydraulic head
103 measurements that correspond to pumping and monitoring in different locations in the
104 aquifer (Gottlieb and Dietrich, 1995; Li et al., 2007). Although it has inherent
105 limitations, as discussed in Bohling and Butler (2010), hydraulic tomography has

been shown to be a capable and effective method for characterising the spatial variability of hydraulic transmissivity in heterogeneous porous media through synthetic, numerical studies (e.g. Yeh and Liu, 2000, Liu et al. 2002; Bohling et al., 2002; Cardiff and Kitanidis, 2008; Hao et al., 2008; Liu and Kitanidis, 2011); laboratory experiments (e.g. Liu et al., 2002; Brauchler et al. 2003; Liu et al., 2007; Illman et al., 2007, 2008) and field experiments (Bohling et al., 2007; Straface et al., 2007; Cardiff et al., 2009; Illman et al. 2009; Berg and Illman, 2011; Brauchler et al. 2011; Huang et al., 2011). In particular, Yeh and Liu (2000), Liu et al. (2002), Hao et al. (2008) and Cardiff et al. (2009) have shown the effectiveness of hydraulic tomography in characterising a heterogeneous field of hydraulic conductivity using only a limited number of steady-state head measurements. In their synthetic study, Hao et al. (2008) have shown that, when multiple series of pumping test data are available in fractured rocks, the highly conductive zones and their connectivity can be successfully imaged using the hydraulic tomography technique. Illman et al. (2009) recently applied a similar approach to a fractured granite in Japan and they obtained high-resolution distributions of both the hydraulic conductivity and storativity by using transient data from two, large-scale, cross-hole pumping tests. Day-Lewis et al. (2000) proposed an approach for characterising high conductive zones in a fractured aquifer in 3D using the simulated-annealing method. Apart from these studies, most of the previous work focuses on characterisation of hydraulic conductivity fields using hydraulic tomography techniques in relatively homogeneous alluvial or fluvial aquifers. To the best of our knowledge, hydraulic tomography techniques have not previously been applied to karstified, fractured aquifers. In these types of aquifers, due to the low intergranular conductivity of the background rock matrix, flow is strongly restricted within a limited number of

interconnecting fractures (Tsang and Tsang et al., 1987). In addition, with the circulation of soluble groundwater through the interconnecting fractures, the original fracture apertures can be further enlarged to generate high-conductivity flow pathways which, in turn, further constrain the flow in the fractured medium (Bodin et al., 2012). Therefore, in order to predict the hydrodynamic behaviour in these systems, it is crucial to accurately characterise the location, distribution and connectivity of the fracture and karstic pathways.

In this work, we focus on characterising the two-dimensional, highly spatially-dependent transmissivity field of the Terrieu hydrogeological experimental site in a fractured and karstified limestone aquifer located to the north of Montpellier, Southern France. Because we aim to resolve the fine-scale characteristics of the transmissivity field, the problem undertaken is essentially a large-scale inverse modelling task, i.e. the dimension of the parameter space is high, which has rarely been addressed in previous hydraulic tomography applications. To handle the high computational demands in the large-scale inverse problem, a sparse nonlinear optimizer (SNOPT; Gill et al., 2008) is applied to 8 sets of steady-state hydraulic head data recorded in 22 observation boreholes during a sequential aquifer test (sequential cross-hole pumping test conducted at various locations) for hydraulic tomography. The inverted transmissivity fields are compared to the statistical fracture data mapped on the outcrops in the vicinity of the test site to check the consistency between the structural anisotropy and flow anisotropy in the fractured and karstified groundwater system at the local scale.

2. Description of the test site and available datasets

154 The Terrieu experimental site, which is situated approximately 15 km north of
155 the city of Montpellier (France), has been set up to investigate the hydrodynamic
156 behaviour in the Lez aquifer which has served as the major water supply for the
157 Montpellier urban area since the mid-19th century. The Lez aquifer is a fractured and
158 karstic reservoir and consists of massive Late Jurassic and Early Cretaceous
159 limestones (Leonardi et al., 2011, Jourde et al., 2014). The hydraulic properties of this
160 aquifer are dominated by the fault system in the area and are complex (Fig.1; Roure et
161 al., 1992; Petit and Mattauer, 1995; Watkinson et al., 2006). The Terrieu site is
162 located between two major faults in the Lez aquifer (Fig. 1). This experimental site is
163 about 1500 m^2 (30 m x 50 m) in size (Fig. 2) and it lies on a local NE-SW trending
164 monocline, with the inclined limb dipping at 15 to 20 degrees toward NW (Jazayeri
165 Noushabadi et al., 2011). The boreholes at the site are vertical and only intersect the
166 upper part of the aquifer consisting of marly limestones of Cretaceous age. The
167 geology at the site comprises two major rock units: the upper unit is composed of
168 inter-bedded, low-permeability marls and marly limestone layers. It has a vertical
169 extension of 30-40 metres and acts as an upper boundary that confines the aquifer.
170 The lithology in the lower unit is more uniform and more massive limestone beds.
171 The total thickness of the unit is unknown because of the maximum drilled depth (60
172 m) of the boreholes.

173 Twenty-two vertical boreholes have been drilled into the aquifer. These
174 boreholes are relatively evenly spaced over the test site area with an average spacing
175 of about 5 m (Fig. 2). This allows detailed investigation of groundwater flow on a fine
176 scale. All of the boreholes are uncased with a diameter of either 0.22 m or 0.33 m.

177 **2.1 Fracture mapping**

178 Detailed fracture mapping on the test site pavement rocks has been conducted
179 by Jazayeri Noushabadi (2009) and later completed by Wang et al. (2014, Fig. 2).
180 Their results indicate that two major fracture sets are present: one oriented ENE-
181 WSW and the other NW-SE. New fracture data collected by the present authors from
182 the areas up- and down-stream of the test site along the Terrieu River are in
183 agreement with the Terrieu pavement fracture database. This work confirms the
184 presence of the two major fracture sets in the local region. The rose diagrams for both
185 the fracture frequency and cumulative length based on the mapped fracture data at all
186 stations have been plotted in the Fig. 3. These diagrams clearly reveal the structural
187 anisotropy at the field site scale. This fracture pattern will be compared to the inverted
188 transmissivity fields in later sections.

189 **2.2 Well logging and packer tests**

190 During last two decades, extensive hydrogeophysical studies have been
191 conducted at the Terrieu site using temperature, electrical conductivity, borehole
192 video loggings and straddle packer tests (Fig. 4 and Fig. 5b). Temperature and
193 conductivity logs were recorded in all the boreholes; videos were recorded in 10
194 boreholes; and packer tests were performed in 5 boreholes. The borehole video data
195 show that the fractures are generally steep and stop preferentially at bedding surfaces.
196 The fractures are oriented in two major directions which are similar to the fracture
197 patterns observed in outcrop on the test site pavement (Fig. 3). This justifies the use of
198 surface fracture data to characterise the fracture network within the underlying unit.
199 In addition, intense karstification has been observed either along major fractures and
200 bedding planes or at the intersections between fracture and bedding planes. When
201 borehole video data are used in conjunction with the temperature and conductivity
202 logs, it is found that the preferential flow paths are strongly restricted within a limited

member of karstified fractures and karst conduits developed along an important, gently tilted, bedding plane. Its depth varies between 25 and 40 m from the site surface in different boreholes (Jazayeri Noushabadi et al., 2011; Fig. 5b). Straddle packer tests further indicate that this open bedding plane (Fig. 4a and Figs. 5b&c) is the most conductive feature which intersects the boreholes over the entire penetrated interval and its transmissivity is found to be more than 3 orders of magnitude higher than that of the other tested intervals. During the tests, injection of water into the intervals that are made up of only matrix was almost impossible confirming that flow in the matrix is negligible. In addition, no evidence of vertical flow has been found on the borehole videos and during packer tests. Similar phenomenon regarding the development of main flow pathways in limestone aquifers have been previously reported by Filipponi et al. (2009), Castagna et al. (2011), Bodin et al. (2012) and many others in the karst community. The observations from the well logging and packer test data form the basis for this work which aims to model the main conduit network in 2D (Fig. 5c).

2.3 Sequential cross-hole pumping tests

Eight cross-hole pumping tests have been performed at the Terrieu site and the pumping rate for each test ranges from 0.2 to 53 m^3/h depending on the well diameter, productivity of the well and pump power limits (Jazayeri Noushabadi et al., 2011). We assume the measurement errors in all the tests are independent and identically distributed by considering a value of 0.01m to include all the measurement errors from equipment, operation and any other unpredictable error sources in nature.

The steady-state head data clearly reveal the highly heterogeneous nature of the study area (Fig. 6). Firstly, pumping in one borehole does not generate drawdowns

in all other observation boreholes even at high pumping rate. For instance, the registered pumping rate in P0 was 53 m^3/h; however, no obvious drawdown was recorded in other boreholes such as P1, P6, P7, P18 and P19. The recorded drawdowns during a pumping test are not evenly distributed with respect to the distance between the pumping and observation wells. For example, although P2 and P7 are located approximately at the same distance to P0, their hydrodynamic response differs greatly: a large drawdown was recorded in P2 (2.2m) but no drawdown was monitored in P7. Moreover, it is also found that pumping in different boreholes, i.e. at different locations in the aquifer, generates significantly different drawdown distributions. In particular, when pumping in P0, many boreholes exhibit large drawdown, regardless of the distance from the pumping well. However, when pumping in P10, the water table drawdown is only observed in a few boreholes close to the pumping well. All of these observations reflect the complex interconnection of the fracture and karst system and highlight the challenges in the prediction of groundwater flow in a fractured and karstic aquifer.

3. Hydraulic tomography

3.1 Forward model

In two-dimension, steady state groundwater flow in an isotropic, heterogeneous and confined aquifer is governed by the following simple continuity and constitutive equations:

$$\nabla \cdot u = Q_s \tag{1}$$

$$u = -T\nabla h \tag{2}$$

that are subject to the following boundary conditions:

$$h = h_D \quad \text{on } \Gamma_D \tag{3}$$

$$-\boldsymbol{n} \cdot T\nabla h = 0 \quad \text{on } \Gamma_N \tag{4}$$

where u represents the Darcy velocity (flux, in m s^{-1}); Q_s (m s^{-1}) represents the hydraulic sources/sinks due to pumping events; T (m^2 s^{-1}) represents transmissivity; h(m) represents hydraulic head; $\boldsymbol{n}$ denotes the unit vector normal to the boundary, Γ_N. Equations (3) and (4) represent the Dirichlet condition imposed on boundary Γ_D and the Neumann boundary condition applied at boundary Γ_N, respectively. The specific boundary conditions used in the models described here will be discussed in detail in the next section.

3.2 Inverse problem

The main objective of inverse modelling in this work is the reconstruction of the spatially distributed hydraulic transmissivity field by matching the simulated hydraulic responses recorded in each borehole with the observations in the corresponding borehole during a set of sequential pumping tests. In order to achieve this goal, we minimise the following objective function with bounds constraints imposed on the transmissivity field:

$$minimize\ \Gamma(\boldsymbol{h}_{\mathrm{f}}, \boldsymbol{s}) = (\boldsymbol{h}_{\mathrm{f}} - F(\boldsymbol{s}))^T \mathbf{R}^{-1} (\boldsymbol{h}_{\mathrm{f}} - F(\boldsymbol{s})) \tag{5}$$

$$\text{Subject for } \boldsymbol{l} \le \boldsymbol{s} \le \boldsymbol{u}$$

where $\boldsymbol{h_f}$ denotes the $n \times 1$ vector of real measurements; $\boldsymbol{s}$ represents the $m \times 1$ vector containing the unknown values of the logarithm of the hydraulic transmissivity, $log_{10}T$; $F(\boldsymbol{s})$ represents the forward problem operator taking a log hydraulic transmissivity field $\boldsymbol{s}$ as input while predicting the $n \times 1$ hydraulic head values; $\boldsymbol{R}$

denotes the $n \times n$ covariance matrix of the measurements errors. l and u are the lower and upper bound vectors respectively for the constraint of the transmissivity field.

Even though some *a priori* information derived from the aquifer tests has been used to define the initial conditions at the initiation of the inversion process, there is no spatial penalty matrix or variogram used to regularise the inversion model. The reason for this is that the inherent extreme heterogeneity and anisotropy of the bedrocks at the field site induced by the fractures and karstic features pose significant uncertainties in estimating the structural parameters such as the variances and correlation lengths of the variogram. Such data are generally easier to define in less heterogeneous and isotropic geological media as described by Cardiff et al. (2009), Cardiff et al., (2012) and Jardani et al. (2012). It is known that the hydraulic inverse problems have non-unique solutions. In order to filter out the reliable solutions, upper and lower limits are often employed to constrain the inversion model and to exclude the undesirable values in the parameter field. These bounds for hydraulic properties are strongly depend on the inherent nature of the heterogeneous geological medium. Consequently, we choose to deal with a bound-constrained problem. The inversion algorithm adopted in this study is the Sparse Nonlinear Optimizer (SNOPT; Gill et al., 2002). This algorithm is a proven gradient-based routine in optimisation and especially effective for solving large-scale, nonlinear problems whose functions and gradients are expensive to evaluate (Jockenhovel et al., 2003; Gill et al., 2005; Cardiff and Kitanidis, 2008; Fowler, 2010). The SNOPT algorithm is efficient for models with a large number of constraints and a moderate number of degrees of freedoms. It computes the exact analytic derivative of the objective and constraint functions using the adjoint method (Gill *et al.,* 2008). These advantages make it suitable for solving distributed hydraulic inverse problems of the type being addressed in this paper,

297 which are nonlinear, ill-posed and underestimated. We note that even in the coarsest
298 model used in this work, the number of hydraulic unknowns reaches to 2160. In such
299 a large-scale inverse problem, the computational costs in computing the Jacobian
300 (sensitivity) matrix and in minimising the objective function are prohibitive and
301 cannot be handled by the classical methods. Therefore the results of our work are of
302 value for the hydraulic characterisation of fractured and karstic aquifers using field
303 data and of revenue to workers in the field of hydraulic characterisation of such
304 aquifers.

305 **3.3 Inversion model setup and convergence performance criteria**

306 The Terrieu site is modelled as a 2D rectangular domain ($60m \times 36m$; Fig. 7).
307 The domain is regularly discretized into square grids. This local model is enclosed by
308 a large buffer region of 1.2 km by 1.2 km in order to reduce the influence of the
309 hydraulic boundaries on the local inverse problem. Geologically, this region also
310 corresponds to the block area between the two major faults running through the Lez
311 aquifer (Fig. 1). Constant hydraulic properties are considered in the buffer region. A
312 no flow boundary condition is applied to the faults and constant head condition is set
313 for the other two boundaries. The initial condition is set in the entire model by
314 assuming a static water table level (30m) prior to each pumping tests.

315 Case tests are designed to investigate the influences of the initial local
316 transmissivity model, local and regional transmissivity bounds, grid sizes, and
317 inversion strategies on the inversion of local transmissivity field. To quantify the
318 inversion performance and monitor the convergence for each inversion model, we
319 calculate both the objective function value at the beginning and the end of the
320 inversion, J_{start} and J_{end}, and the root mean square, $RMS = \sqrt{\frac{J_{end}}{N}}$, where N is the

number of measurements used in the inversion model. Generally, if the condition $0 < RMS < 1$ holds, the inversion converges while if $RMS > 1$ holds, the inversion is not converge.

3.4 Validation of the inversion methodology: a synthetic case study

Prior to field application, synthetic experiments were set up to test the feasibility and effectiveness of applying the proposed methodology for detecting the highly conductive zones and their quantifying their connectivity. We generated three sets of discrete fractures restricted to the regions around the borehole using the mapped Terrieu fracture data. A karstic conduit, which passes through the test domain, was placed manually in the model. The real locations of the Terrieu boreholes were used for positioning the boreholes in the DFN model. This created three types of borehole-network connectivity (Fig. 8a), and the model was used to perform synthetic pumping tests. In the synthetic experiments, the matrix flow is simulated by using Darcy's law (Eq. 2), whereas the fluid velocity through the discrete fractures and the karst channel is calculated using the cubic law (Witherspoon et al., 1980; Jourde et al., 2002b):

$$u_d = \frac{a_p^2}{12}\frac{\rho g}{\mu}\nabla \mathrm{h} \tag{6}$$

where u_d (m s^{-1}) is the Darcy velocity (flux) through each discrete feature (a fracture or a karst conduit); h is the hydraulic head (in m); a_p (m^{-1}) denotes the aperture of individual fractures or karst channel; ρ (kg m^{-3}) denotes the fluid density; μ (kg m^{-1} s^{-1}) denotes the fluid dynamic viscosity; g (m s^{-2}) is the acceleration of gravity. Values of 1 mm, 20 mm, 10^{-8} m^2s^{-1} and 10^{-5} m^2s^{-1} were set for the apertures of discrete fractures and

karst conduit, and the transmissivities of matrices in the local and regional areas, respectively. Real pumping rates was used to conduct the synthetic studies.

Inversion of these tests was performed on two regularly discretised models with grid sizes of 1m by 1m and 0.5m by 0.5m, respectively (Fig. 8b and Fig. 8c). As expected, both models achieved good convergence (Fig. 9) and it can be seen that, in general, the hypothetical fracture pattern was successfully resolved by the inversion: the connectivities between the karst channel and the fracture clusters, and between the boreholes and different flow regions (i.e. karst, fracture or matrix) were all preserved. For instance, boreholes P0, P2, P8, P12, P15, P11 and P20 were assumed to sit on the karstic channel, and similar connections were captured in the inverted transmissivity fields (Fig. 8b and Fig. 8c). Good agreement was also found when the boreholes were connected to the fractures or the matrix. In addition, a comparison between Fig. 8b and Fig. 8c indicates that a more reliable transmissivity distribution was obtained by using a finer grid. These results confirm the capability of the proposed hydraulic tomography method to determine the distribution of the main conductive conduits and characterise their connectivity.

4. Application: inversion of Terrieu site pumping test data

4.1 Case 1: Influence of initial model on the inversion results

Fig. 10 shows two resulting transmissivity fields reconstructed using the same hydraulic head measurements but with different initial models. In the first inversion model (Fig. 10a), a constant transmissivity value of ($10^{-4}\ m^2 s^{-1}$) was set for both the regional and local areas. We use this value because it is a typical transmissivity for fractured and karstified aquifers and it is also consistent with the interpretation of single-hole test data given by Jazayeri Noushabadi (2011). However, in the second

inversion model (Fig. 10b), an initial transmissivity field as shown in Fig. 7 was adopted for the local region and the same constant transmissivity value as in the first inversion model (Fig. 10a) was applied to the regional area. This initial model was derived from the connectivity interpretations based on the cross-hole pumping tests at the site. Both tests were realised with the same grid size of 1 m by 1m and the same range of $[10^{-8}, 10^{-1}]$ $(m^2 s^{-1})$ for constraining the local transmissivity values.

As it can be seen, both models converged and, even though slightly different, good fitness of the inverted and measured hydraulic data was obtained for both models (Fig. 11). Despite the fact that highly heterogeneous transmissivity fields were predicted by both the inversion models, the spatial patterns of the resulting transmissivity fields are significantly different. Using a constant initial transmissivity in the entire inversion model, the vast majority of cells within the imaged local transmissivity field tend to be filled with extremely high or low values of the given local transmissivity range. Only a few cells, which are primarily located around the boreholes, have moderate transmissivity values (Fig. 10a). In other words, the resulting transmissivity field in this case tends to be binary with high and low values. In contrast, a more diffused, heterogeneous pattern of transmissivities is calculated when the initial transmissivity field (Fig. 7) was used in the inversion (Fig. 10b). It is also noted that, when this initial transmissivity field is considered, the inversion resolved more continuous NE-SW trending and relatively less NW-SE trending conductive structures, which is more consistent with the fracture statistics shown in the Fig. 3.

Unlike many previous geostatistical studies in which *a priori* knowledge derived from hydrogeological or hydrogeophysical measurements were integrated into the objective function as a penalty criteria to regularise the parameter field, in this

work, the inter-well connection information was used only as an initial condition to trigger the inverse modelling. We note that the well connection data were integrated in the initial models (Fig. 7) merely through subjective interpretations. More rational integration of connectivity data can be achieved by applying the simulated annealing method proposed by Day-Lewis (2000) or the method of Carle and Fogg (1997) which is based on transition probability geostatistics. Applications of these methods require the use of a considerably large number of field measurements to condition the geostatistical simulations. Nevertheless, even in these relatively simple models (Fig. 7), the comparison of the calculated transmissivity fields in Fig. 10 still reveals the influence of the use of the inter-well connection information in guiding the gradient-inverse modelling in fractured media. Adopting the *a priori* connection information as an initial condition in the inversion produces transmissivity patterns which are more consistent with the fracture data. Accordingly, we believe the results obtained from this approach are more realistic and reliable. In the remaining discussion, the same initial transmissivity field presented in Fig. 7 is used in the inversion simulations.

4.2 Case 2: Influence of transmissivity bounds for the regional and local regions on the inversion results

4.2.1 Bounds for the regional bulk transmissivity

The reconstruction of the hydraulic transmissivity field of the local domain is affected by regional transmissivity because the interconnecting fractures and karst channels have developed beyond the studied domain, which is demonstrated by the high productivity of the P0 borehole. We considered a range of [-5, -2] to represent the range of the logarithm of the transmissivity, $\log_{10}\mathrm{T}\,(m^2s^{-1})$, in the regional buffer area which encloses the local model. Within the local region, the same

transmissivity range of [10^{-8}, 10^{-1}](m^2s^{-1}), was set as in previous inversion models discussed.

It is found that over the range of [-4, -2] for the log regional transmissivity, there is a good correlation of the hydraulic head data, and in addition, good convergence performances have been achieved (Fig. 13; Table 1). The inverted local T patterns in these models are generally similar (Fig. 12a, Fig. 12b and Fig. 12c). However, outside the range, both the convergence performance and fitting of head data becomes much worse (Fig. 13d; Table 1). Notice that when the value -2 is used, although the inversion model still converged, the value of the objective function at the end of the inversion for this model is about 10 times higher than that when a value in the range of [-4, -3] is adopted. This indicates that this value (T = 10^{-2} m^2s^{-1}) is not the best value to be considered for the large-scale regional transmissivity. The analysis done by Jazayeri Noushabadi et al. (2011) on the regional pulse test data indicates that the highest estimated permeability value is around 50000 mD at the kilometre scale. This permeability corresponds to a transmissivity value of $10^{-2}(m^2s^{-1})$, if it is assumed that the effective height for flow is 20 m. However, the true effective height for flow in the Terrieu site is far smaller, i.e. the major groundwater flow is found to be strongly constrained within the intensely karstified bedding plane with a largest opening of only about 20 cm. The flow through the intergranular matrix is very limited because of the extremely low permeability of the tight limestones in the Terrieu field site area. All of the former hydrogeological investigations, now supported by the inversion result, lead us to believe that the upper bound for the regional bulk transmissivity is less than $10^{-2}(m^2s^{-1})$. However, as can be seen from the inversion results (Fig. 13d), the regional transmissivity value cannot be as low as $10^{-5}(m^2s^{-1})$. When this low value was used to represent the

441 transmissivity in the buffer region, the inversion model did not converge and in
442 addition, the fit between inverted and measured, steady-state, head data was much
443 worse. Therefore, in our opinion, the small range of [-4, -3] for the log regional
444 transmissivity is appropriate and probably gives a good estimate of the regional scale
445 equivalent transmissivity.

446 It can be seen from Fig. 13d that, among all the test data, the use of low
447 regional transmissivity exerts more impact on the head data of the P0 test and the
448 inverted hydraulic heads are systematically lower than the measured heads. This
449 suggests that P0 well may connect to the main flow path existing on the regional scale
450 and pumping in this well reflects regional hydrodynamic properties. When the
451 regional bulk transmissivity is given a much lower value than the real averaged
452 transmissivity, there is not enough water supply from the regional area. This results in
453 larger drawdowns in most of the observation boreholes in the inversion model.

454 **4.2.2 Bounds for the local, spatially varying transmissivities**

455 It is also known that changing the constraining bounds of local transmissivity
456 values may also affect the inversion results. To investigate this issue, we considered
457 five different sets of bounds, i.e. [-10, -1], [-8, -1], [-7, -2], [-6, -3] and [-5, -4], for the
458 log transmissivity values in the local system. In all the five inversion models, a
459 constant value of $10^{-4}(m^2 s^{-1})$ was assigned to the transmissivity in the buffer region.

460 It can be seen that good data-fits are obtained for the large ranges of [-10, -1]
461 and [-8, -1] (Fig. 15 and Table 2). However, as the range becomes smaller, which
462 means the local transmissivity field is forced to be more homogeneous, both the
463 correlation of inverted and measured head data and the inversion convergence become
464 progressively worse (Table 2). Thus, if it is assumed that the heterogeneity of the

transmissivity field is low in a region where it is in fact high (for example at the Terrieu site as has been shown from former hydrodynamic and geological investigations), a misfit would be expected between the predicted and observed values of hydraulic head. In addition, the inverted transmissivity fields show significantly different flow patterns (Fig. 14 and Fig. 10b). In general, as the range applied to constrain the spatial variability of local transmissivities becomes smaller, the resolved flow features become larger, and more randomly oriented, deviating from the observational data. It is also noted that, on the transmissivity maps shown in Fig. 14b and Fig. 14c, more conductive features were depicted in the areas that are not constrained by any borehole measurements, e.g. the massive conductive zones resolved in the lower-middle and lower-right areas of Fig. 14b and the upper-left area of Fig. 14c. All of these results confirm the extremely heterogeneous nature of the fractured and karstified limestones of the field site. It is clear that when the local domain is assumed to be more homogeneous, we obtained poor representations of the transmissivity fields with high uncertainties.

In summary, in order for the inversion model to represent the observed hydraulic behaviour of the fractured and karstified system in the Terrieu site, a large range of transmissivities, $[10^{-8}, 10^{-1}](m^2 s^{-1})$, is required within the local system and a smaller range of $[10^{-4}, 10^{-3}](m^2 s^{-1})$ is needed for the bulk transmissivity in the buffer region. Having determined the range of transmissivity over which a good correlation exist between the measured hydraulic head and that predicted by the model, the uncertainties in quantification of the flow properties in the study area are dramatically reduced. The difference in the transmissivity ranges on the local and regional scales may also reflect the scaling of the flow properties of the studied flow network. As can be seen from Fig. 13 and Fig. 15, on a regional scale, the range of

transmissivity is smaller compared with the range of transmissivity for the local scale. In other words, the flow is highly heterogeneous on the local scale while the flow appears to be more homogeneous as the scale increases and reaches the REV of the studied flow network. If this relationship is persistent in the study area, it should be possible to determine a support scale of the REV for the multi-scale fractured system.

4.3 Influence of the grid size on the inversion results

Fig. 16 presents two transmissivity fields reconstructed by using different grid sizes: 0.5m by 0.5m and 0.25m by 0.25m. These transmissivity fields can be further compared to the Fig. 10b, which uses a grid size of 1m by 1m. A local transmissivity range of $[10^{-8}, 10^{-1}](m^2 s^{-1})$ and a regional transmissivity value of $10^{-4}(m^2 s^{-1})$ are considered in these models.

When the transmissivity patterns of Fig. 10b and Fig.16a are compared it can be seen that the use of a smaller grid allows more fine-scale flow structures to be resolved by the inversion using the same set of field data. The flow pattern inferred from the transmissivity field predicted on the finer scale is apparently more localised and restricted to few conductive conduits. Even though, at a first glance, the transmissivity field shown in the Fig. 10b looks different to that presented in the Fig. 16, many high-conductivity paths can be seen on both transmissivity fields at similar locations. For instance, the large continuous path between the P21 and P8 wells, as well as some local, smaller conduits in the triangular region defined by wells P8, P16 and P19 are common features shared by the two transmissivity fields. In addition, a similar connectivity pattern between some boreholes, e.g. P2-P9, P4-P10, P6-P7, P8-P21, is also captured by both grid sizes. These consistencies between the resulting transmissivity fields on different scales show that even with a limited number of

514 steady-state field measurements, the highly parameterised inversion models are still
515 capable of providing reliable and realistic results.

516 Regarding the inversion performance and computational efforts, the inversion
517 model using a grid size of 1m by 1m ran for about 1 hour and converged. The
518 inversion model with a grid size of 0.5m by 0.5m ran for about 8 hours and also
519 converged. However, the last inversion model in this series, with a grid size of 0.25m
520 by 0.25m, ran for two days, until the pre-defined maximum number of objective
521 function evaluations was reached but the inversion did not converge. An additional
522 inversion run was performed for this last model and a higher value for the number of
523 objective function evaluations was set. The inversion model ran for about three and
524 half days but unfortunately it still did not converge. Generally, it is found that as the
525 grid size becomes smaller, a major mismatch between the prediction and the observed
526 behaviour occurs (Fig. 11b and Fig. 17). Two possible reasons for this are: firstly,
527 from the geological point view, it may reflect the fact that the grid size, i.e. 0.25m, is
528 close to or falls below the scale of the major features (these are as large as 0.2-0.3m as
529 can be seen in the borehole video data; see Fig. 4 for reference) controlling the
530 groundwater flow. Alternatively, from the point of view of numerical calculation, this
531 reduction of grid size from 1m by 1m to 0.25m by 0.25m may have led the model
532 being over-discretised thereby reaching the limit of the SNOPT algorithm in solving
533 the overestimated nonlinear inverse problem. In addition when a finer grid size is
534 used, the complexity of the inverse problem may overwhelm the sparse database
535 employed to constrain the problem. It follows that when limited field data are
536 available it is important to determine the appropriate parameterisation when
537 modelling highly heterogeneous fractured/karstified aquifers.

538 **6. Conclusions**

539 Modelling of the groundwater flow in the fractured and karstified aquifers is
540 inherently a challenge because of the nature of the extremely high heterogeneity and
541 anisotropy of the systems and the scarcity of field measurements. However, by careful
542 selection of the modelling approach and coupling inversion techniques, we can still
543 obtain reliable results with the available data set. We applied hydraulic tomography to
544 jointly analyse eight sets of cross-hole pumping tests based on a simple, regularly-
545 parameterised equivalent porous medium model and demonstrated the ability of this
546 method to estimate the transmissivity field of a test site located within a real fractured
547 and karstified aquifer. We note that the modelling task undertaken in this paper
548 involved solving a large-scale inverse problem where the computational demands are
549 heavy. Such large-scale inverse problems have rarely been addressed in the water
550 resources literature, except for some recent work conducted by Kitanidis and co-
551 workers (e.g. Lee and Kitanidis, 2014). However, we recognise that results were
552 achieved by using a dense borehole network in a limited area and an extensive
553 hydraulic dataset, even though the hydraulic data are still apparently sparse compared
554 to the large number of hydraulic unknowns (2160 in the coarsest model) in the large-
555 scale inverse problem addressed in this work. This may imply that based only on this
556 case study it is difficult to claim that the hydraulic tomography technique is a
557 generally applicable method for aquifer characterisation in fractured media and that
558 its applicability need to be further tested using other datasets.

559 Results have shown that the use of the initial connectivity information derived
560 from pumping tests significantly improves the inversion results. It was also found that
561 in order for the inversion models to represent the observed behaviour of the system, a
562 large range of transmissivities, $[10^{-8}, 10^{-1}](m^2s^{-1})$, is required within the local
563 system and a smaller range of $[10^{-4}, 10^{-3}](m^2s^{-1})$ is needed for the bulk

transmissivity in the buffer region. A series of spatially distributed transmissivity fields that produce similar hydraulic behaviours to the real pumping tests were obtained. These transmissivity fields allow the identification of the preferential flow paths that are complexly organised within the low-permeability background matrix. A predominate NE-SW flow direction was identified. These inverted transmissivity fields are believed to be reliable and representative for the Terrieu site since they are consistent with the hydrodynamic and geological measurements gathered there. However, since solute transport data is not integrated in the model condition practise we acknowledge that the inverted heterogeneous field can only be used for pressure and flow predictions. It may completely fail for predicting tracer concentrations. Obtaining a more plausible characterisation of the site heterogeneity may require joint inversion of piezometric data and other data such as solute concentration, electrical and geophysical data. The methodology of joint inversion of piezometric and solute concentration data collected at the Terrieu site is currently being conceived and will be addressed in the future work.

Even though the regularly parameterised model used in this study is seemingly oversimplified and might not be considered appropriate for modelling the complex flow path network in the intensely fractured and karstified system observed at the field site scale, it possesses the flexibility to characterise the spatial location and connectivity of the main flow paths. In future work, it will be useful to apply derivative-free methods such as the Markov chain Monte Carlo (McMC) approach to take into account the non-uniqueness solution and the uncertainties of the inverse modelling. The inversion results and effectiveness of both the gradient-based and derivative-free approaches could then be compared. Furthermore, as the fracture network at the Terrieu site has been mapped and statistically characterised, it would

be worth constructing a set of DFN/DFM models and to apply the hydrodynamic datasets used in this work to condition them to invert the distribution of aperture for fractures in the network. Such approaches would not only allow the major controls of the geometry and connectivity of the main flow paths to be determined, but would also enable the complex channelling behaviour of multiphase flow that may have a major impact in fractured oil/gas reservoirs on the fluid exchange between the conductive flow paths and the bulk fracture rock, to be captured.

Acknowledgements

This work was performed within the framework of the MEDYCYSS observation site, part of the KARST observatory network (www.sokarst.org) initiated by the INSU/CNRS, which aims to strengthen knowledge-sharing and to promote cross-disciplinary research on karst systems. We acknowledge funding from Total for the PhD project of the first author. We thank the reviewers for providing useful comments which improve this paper.

References

Adler, P.M., Thovert, J.-F., 1999. Fractures and Fracture Networks. Theory and Applications of Transport in Porous Media. *Kluwer Academic Publishers, Dordrecht, the Netherlands, 429 pp.*

Berg, S.J., and Illman, W.A., 2011. Three-dimensional transient hydraulic tomography in a highly heterogeneous glaciofluvial aquifer-aquitard system. *Water Resources Research, Vol. 47, W10507, doi: 10.1029/2011WR010616.*

Berkowitz, B., 2002. Characterizing flow and transport in fractured geological media: a review. *Advances in Water Resources 25, 861–884.*

Bodin, J., Ackerer, P., Bosisson, A., Bourbiaux, B., Bruel, D., de Dreuzy, J., Delay, F., Porel,

G. and Pourpak, H, 2012. Predictive modeling of hydraulic head responses to dipole flow experiments in a fractured/karstified limestone aquifer: insights from a comparison of five modeling approaches to real-field experiments. *Journal of Hydrogeology. 454-455 (2012) 82-100*.

Bohling, G. C., X. Zhan, J. J. Butler Jr., and L. Zheng (2002), Steady shape analysis of tomographic pumping tests for characterization of aquifer hetero- geneities, *Water Resources Research, 38(12), 1324, doi:10.1029/2001WR001176*.

Bohling, G.C., and J.J., Jr. Butler, (2010), Inherent limitations of hydraulic tomography, *Ground Water*, vol. 48, no. 6, p. 809-824,doi:10.1111/j.1745-6584.2010.00757.x

Brauchler, R., R. Hu, P. Dietrich, and M. Sauter (2011), A field assessment of high resolution aquifer characterization based on hydraulic travel time and hydraulic attenuation tomography, *Water Resources Research, 47*, W03503, doi:10.1029/2010WR009635.

Brauchler, R., R. Liedl, and P. Dietrich (2003), A travel time based hydraulic tomographic approach, *Water Resources Research*, 39(12), 1370, doi:10. 1029/2003WR002262.

Bulter, J.J., McElwee, C.D. and Bohling, G.C., 1999. Pumping tests in networks of multilevel sampling wells: motivation and methodology, *Water Resources Research, 35, 3553-3560.*

Butler, J. J., Jr., and W. Z. Liu, Pumping tests in nonuniform aquifers: the radially asymmetric case, *Water Resources Research, 29(2), 259–269, 1993*.

Cardiff, M. and Kitanidis, P.K., 2008. Efficient solution of nonlinear, underdetermined inverse problems with a generalized PDE model, *Computers & Geosciences, 34 (2008) 1480-1491, doi:10.1016/j.cageo.2008.01.013*.

Cardiff, M., W. Barrash and P. K. Kitanidis (2012). A field proof-of-concept of aquifer imaging using 3D transient hydraulic tomography with temporarily-emplaced equipment. *Water Resources Research* 48: W05531.

Cardiff, M., W. Barrash, P. K. Kitanidis, B. Malama, A. Revil, S. Straface, and E. Rizzo

(2009), A potential-based inversion of unconfined steady-state hydraulic tomography, *Ground Water*, *47*(2), 259–270, doi:10.1111/ j.1745-6584.2008.00541.x.

Carle, S.F., and G.E., Fogg, Modelling spatial variability with one and multi-dimensional Markov chains: Mathematical Geology, v. 29, p. 891-918.

Castagna, M., M. Becker, and A. Bellin (2011), Joint estimation of transmissivity and storativity in a bedrock fracture, *Water Resources Research*, 47, W09504, doi:10.1029/2010WR009262.

Cooper, H.H., Jr., and C.E. Jacob, (1946), A generalized graphical method for evaluating formation constants and summarizing well-field history, *Eos Trans. AGU, 27*(4), 526–534.

Day-Lewis, F.D, Hsieh, P.A. and Gorelick., S.M., 2000. Identifying fracture-zone geometry using simulated annealing and hydraulic-connection data. *Water Resources Research, Vol. 36, No. 7, 1707-1721, July 2000.*

Dershowitz, W.S., and H.H. Einstein, 1988. Characterizing Rock Joint Geometry with Joint System Models. *Rock Mechanics and Rock Engineering Vol. 1, No. 1, 21-51*.

Filipponi, M., Jeannin, P.Y., Tacher, L., 2009. Evidence of inception horizons in karst conduit networks. *Geomorphology 106 (1–2), 86–99*.

Fowler, D., 2010. A synthetic analysis of integrated data fusion: combing hydrologic and geophysical data collected during a tracer test to estimate aquifer flow and transport parameters. *MSc thesis, Clemson University*.

Gill P. E., Murray W. and Saunders M. A. (2002) SNOPT: An SQP Algorithm for Large-scale Constrained Optimization. *SIAM J. Optimisation 12 979–1006.*

Gill, P. E., Murray, W. and Sanders, M. A., 2005. SNOPT: an SQP algorithm for large-scale constrained optimization. *SIAM Review, Vol. 47, No.1, 2005*.

Gill, P.E., Murray, W. and Sanders, M. A., 2008. User's Guide for SNOPT version 7: software for large-scale nonlinear programming.

663 Gomez-Hernandez, J. J., Sahuquillo, A. and Capilla, J. E., Stochastic simulation of
664 transmissivity fields conditioned to both transmissivity and piezometric data, 1. Theory,
665 *Journal of Hydrology*, 203, 163–174, 1997.

666 Gottlieb, J., and P. Dietrich (1995), Identification of the permeability distribution in soil by
667 hydraulic tomography, *Inverse Problems, 11, 353– 360, doi:10.1088/0266-5611/11/2/005*.

668 Gringarten, A.C., 1984. Interpretation of tests in fissured reservoirs and multilayered
669 reservoirs with double-porosity behavior: theory and practice. *SPE paper 10044*.

670 Hao, Y., T.-C. J. Yeh, J. Xiang, W. A. Illman, K. Kenichi, K. C. Hsu, and C. H. Lee (2008),
671 Hydraulic tomography for detecting fracture zone, *Ground Water*, *46*(2), *183–192*,
672 *doi:10.1111/j.1745-6584.2007.00388.x*.

673 Huang, S.-Y., J.-C. Wen, T.-C. J. Yeh, W. Lu, H.-L. Juan, C.-M. Tseng, J.-H. Lee, and K.-C.
674 Chang (2011), Robustness of joint interpretation of sequential pumping tests: Numerical and
675 field experiments, *Water Resources Research, 47, W10530, doi:10.1029/ 2011WR010698.*

676 Illman, W. A. (2014), Hydraulic Tomography Offers Improved Imaging of Heterogeneity in
677 Fractured Rocks. Groundwater, 52: 659–684. doi: 10.1111/gwat.12119

678 Illman, W. A., A. J. Craig, and X. Liu, (2008), Practical issues in imaging hydraulic
679 conductivity through hydraulic tomography, *Ground Water*, 46(1), 120-132. doi:
680 10.1111/j.1745-6584.2007.00374.x.

681 Illman, W. A., X. Liu, and A. Craig (2007), Steady-state hydraulic tomogra- phy in a
682 laboratory aquifer with deterministic heterogeneity: Multime- thod and multiscale validation
683 of K tomograms, *Journal of Hydrology*, *341*(3–4), 222–234,
684 doi:10.1016/j.jhydrol.2007.05.011.

685 Illman, W. A., X. Liu, S. Takeuchi, T.-C. J. Yeh, K. Ando, and H. Saegusa (2009), Hydraulic
686 tomography in fractured granite: Mizunami under-ground research site, Japan, *Water*
687 *Resources Research, 45, W01406, doi:10.1029/ 2007WR006715*.

688 Jardani, A., Dupont, J.P., Revil, A., Massei, N., Fournier, M. and Laignel, B., 2012.
689 Geostatistical inverse modeling of the transmissivity field of a heterogeneous alluvial aquifer
690 under tidal influence. *Journal of Hydrology. 472-473 (2012) 287-300*.

691 Jazayeri Noushabadi, M.R., 2009. Characterization of relationship between fracture network
692 and flow-path network in fractured and karstic reservoirs. *PhD thesis, Universite Montpellier*
693 *II*.

694 Jazayeri Noushabadi, M.R., Jourde, H. and Massonnat, G., 2011. Influence of the observation
695 scale on permeability estimation at local and regional scales through well tests in a fractured
696 and karstic aquifer (Lez aquifer, Southern France). *Journal of Hydrology, 403, 321-336,*
697 *doi:10.1016/j.jhydrolo.2011.04.013*.

698 Jockenhovel, T., Biegler, L.T., Wachter, A., 2003. Dynamic optimization of the Tennessee
699 Eastman process using the OptControlCentre. *Computers and Chemical Engineering 27,*
700 *1513–1531*.

701 Jourde H., A. Lafare, N. Mazzilli, G. Belaud, L. Neppel, N. Doerfliger, F. Cernesson (2014)
702 Flash flood mitigation as a positive consequence of anthropogenic forcings on the
703 groundwater resource in a karst catchement, *Environmental Earth Sciences, 71, 573–583*

704 Jourde, H., F. Cornaton, S. Pistre, P. Bidaux (2002b) Flow behaviour in a dual fracture
705 network. *Journal of Hydrology*, v. 266, p. 99-119, doi:10.1016/S0022-1694(02)00120-8.

706 Jourde, H., S. Pistre, P. Perrochet, and C. Drogue, (2002a), Origin of fractional flow
707 dimension to a partially penetrating well in stratified fractured reservoirs: new results based
708 on the study of synthetic fracture networks. *Advances in Water Resources*, v. 25, p. 371-387,
709 doi: 10.1016/S0309-1708(02)00010-6.

710 Kuniansky, E.L., Bellino, J.C. and Dixon, J.F., 2012. Transmissivity of the Upper Floridan
711 aquifer in Florida and parts of Georgia, South Carolina, and Alabama. U.S. Geological survey
712 groundwater resources program. http://pubs.usgs.gov/sim/3204

713 Lee, J., and P. K. Kitanidis (2014), Largescale hydraulic tomography and joint inversion of
714 head and tracer data using the Principal Component Geostatistical Approach (PCGA), *Water*
715 *Resources Research*, 50, 5410–5427,doi:10.1002/2014WR015483.

716 Leonardi V., Tissier G., Jourde H., 2011 Eléments de génèse des karsts péri-méditerranéens :
717 impact de la tectonique sur l'évolution des drains karstiques (Karsts Nord-Montpelliérains).
718 *Proc. H2Karst, 9th Conference on Limestone Hydrogeology, Besançon (France) 1-3 sep.*
719 *2011, p. 293-296.*

720 Li, W., A. Englert, O. A. Cirpka, J. Vanderborght, and H. Vereechen (2007), Two-
721 dimensional characterization of hydraulic heterogeneity by multiple pumping tests, *Water*
722 *Resources Research, 43, W04433, doi:10.1029/ 2006WR005333.*

723 Liu, S., T.-C. J. Yeh, and R. Gardiner (2002), Effectiveness of hydraulic to- mography:
724 Sandbox experiment, *Water Resources Research, 38(4), 1034, doi:10.1029/2001WR000338.*

725 Liu, X., and P. K. Kitanidis (2011), Large-scale inverse modeling with an application in
726 hydraulic tomography, Water Resources Research, 47, W02501, doi:10.1029/2010WR009144.

727 Liu, X., W. A. Illman, A. J. Craig, J. Zhu, and T.-C. J. Yeh (2007), Labora- tory sandbox
728 validation of transient hydraulic tomography, Water Resources Research, 43, W05404,
729 doi:10.1029/2006WR005144.

730 Long, J.C.S., Remer, J.S., Wilson, C.R., and Witherspoon, P.A., 1982. Porous media
731 equivalents for networks of discontinuous fractures. *Water Resources Research, Vol 18, No. 3,*
732 *645-658.*

733 Matthai, S.K. and Belayneh, M. (2004). Fluid flow partitioning between fractures and a
734 permeable rock matrix. *Geophysical Research Letters 31: doi: 10.1029/2003GL019027. issn:*
735 *0094-8276.*

736 Neuman, S. P. (1987), Stochastic continuum representation of fractured rock permeability as
737 an alternative to the REV and fracture network concepts, in Rock Mechanics: *Proceedings of*
738 *the 28th U.S. Symposium, edited by I. W. Farmer et al., pp. 533–561, A.A. Balkema,*

Rotterdam, Netherlands.

Neuman, S.P., 2005. Trends, prospects and challenges in quantifying flow and transport through fractured rocks. *Hydrogeology Journal. 13 (1), 124–147.*

Petit, J. P. and Mattauer, M., 1995. Palaeostress superimposition deduced from mesoscale structures in limestone: the Matelles exposure, Languedoc, France. *Journal of Structural Geology. Volume 17, Issue 2, pp. 245–247, 249–256*.

Roure, F., Brun, J. P., Colletta, B. and Van Den Driessche, J., 1991. Geometry and kinematics of extensional structures in the Alpine Foreland Basin of southeastern France. *Journal of Structural Geology. Vol. 14, No. 5, pp. 503 – 519.*

Straface, S., T.-C. J. Yeh, J. Zhu, S. Troisi, and C. H. Lee (2007), Sequential aquifer tests at a well field, Montalto Uffugo Scalo, Italy, *Water Resources Research*, *43*, W07432, doi:10.1029/2006WR005287.

Theis, C. V. (1935), The relation between lowering the piezometric surface and the rate and duration of discharge of a well using ground water stor- age, *Eos Trans. AGU, 16*, 519–524.

Tsang, Y. W. and Tsang, C. F., 1987. Channel model of flow through fractured media, *Water Resource Research, Vol. 23, No. 3, 467-479.*

Wang, X., Dausse, A., Cosgrove, J., Jourde, H., Gosselin, O., Lonergan, L., Leonardi, V. and Massonnat, G., 2014. Integrating outcrop fracture data and pressure transient data for constructing local scale flow models in a karst aquifer. *Proceedings, Karst Without Boundaries, 11-15*.

Watkinson, J. and Ward, E. G., 2006. Reactivation of pressure-solution seams by a strike-slip fault sequential, dilational jog formation and fluid flow. *AAPG Bulletin, V. 90, No. 8 (August 2006), P. 1187 – 1200.*

White, W.B., 2002. Karst hydrology: recent developments and open questions. *Engineering Geology 65 (2002) 85-105*.

764 Witherspoon, P.A., Wang, J.S.Y., Iwai, K. and Gale, J.E., 1980. Validity of cubic law for
765 fluid flow in a deformable rock fracture. *Water Resources Research, 16, 6, 1016-12024*.

766 Yeh, T.-C. J., and S. Liu (2000), Hydraulic tomography: Development of a new aquifer test
767 method, *Water Resources Research*, 36(8), 2095–2105, doi:10.1029/2000WR90.

768 Younger, P.L., 1993. Simple generalized methods for estimating aquifer storage parameters.
769 *Engineering Geology, 26, 127-135*.

Tables

Table 1. Inversion performance of regional transmissivity bounds tests

log(T)	Inversion performance	
	J_end	Root mean square (RMS)
-2	102.9	0.97
-3	24.8	0.47
-4	16.9	0.39
-5	3530.5	5.67

Note: all the tests used the initial transmissivity field shown in Figure 6 as initial condition thus in all cases, J_start = 4099336

Editable version:

Table 1. Inversion performance of regional transmissivity bounds tests

log(T)	Inversion performance	
	J_end	Root mean square (RMS)
-2	102.9	0.97
-3	24.8	0.47
-4	16.9	0.39
-5	3530.5	5.67

Note: all the tests used the initial transmissivity field shown in Figure 6 as initial condition thus in all cases, J_start = 4099336

2 column fitting table

Table 2. Inversion performance of local transmissivity bounds tests

log(T) range	Inversion Performance	
	J_end	Root Mean Square (RMS)
(-10, -1)	26.5	0.49
(-8, -1)	16.9	0.39
(-7, -2)	2208.9	4.48
(-6, -3)	14879.5	11.63
(-5, -4)	18856.4	13.09

Note: all the tests used the initial transmissivity field shown in Figure 6 as initial condition thus in all cases, J_start = 4099336

11

12 *Editable version:*

13 Table 2. Inversion performance of local transmissivity bounds tests

log(T) range	Inversion performance	
	J_end	Root mean square (RMS)
(-10, -1)	26.5	0.49
(-8, -1)	16.9	0.39
(-7,-2)	2208.9	4.48
(-6,-3)	14879.5	11.63
(-5,-4)	18856.4	13.09

14

15 Note: all the tests used the initial transmissivity field shown in Figure 6 as initial

16 condition thus in all cases, J_start = 4099336

17 2 column fitting table

18

19

Figures

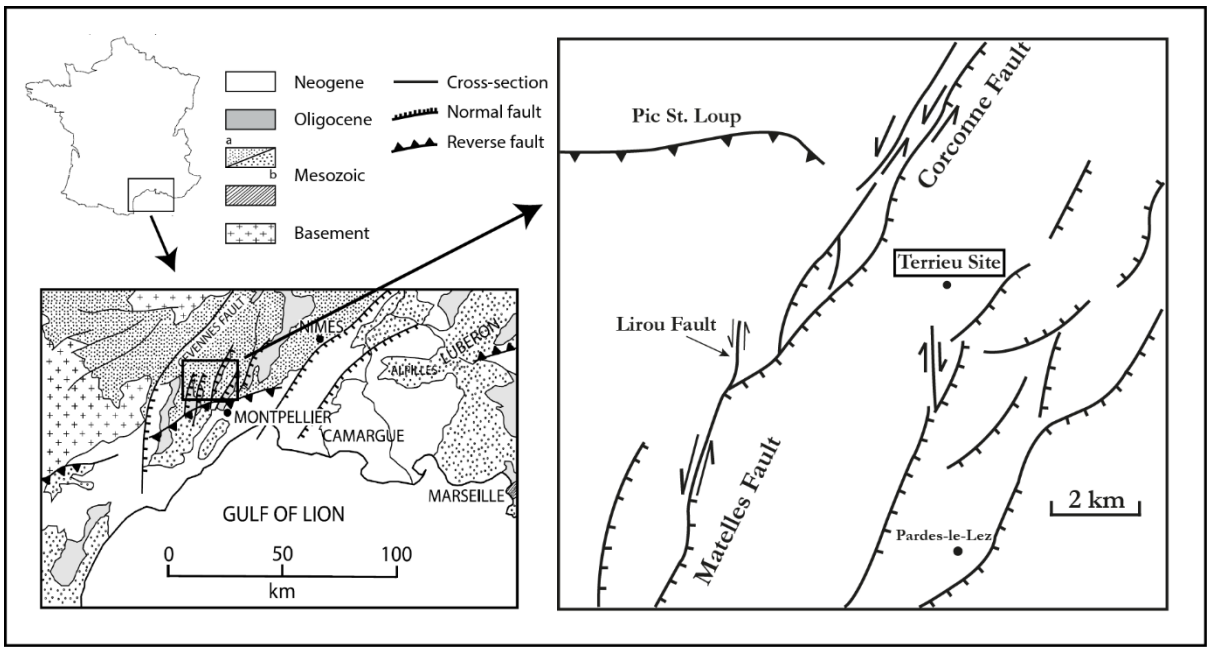

Fig. 1. Geological settings of the study area. The Terrieu experimental site, black rectangle, is the main study area; modified after Roure et al., 1992; Petit and Mattauer, 1995; and Watkinson et al., 2006.

2 column fitting image

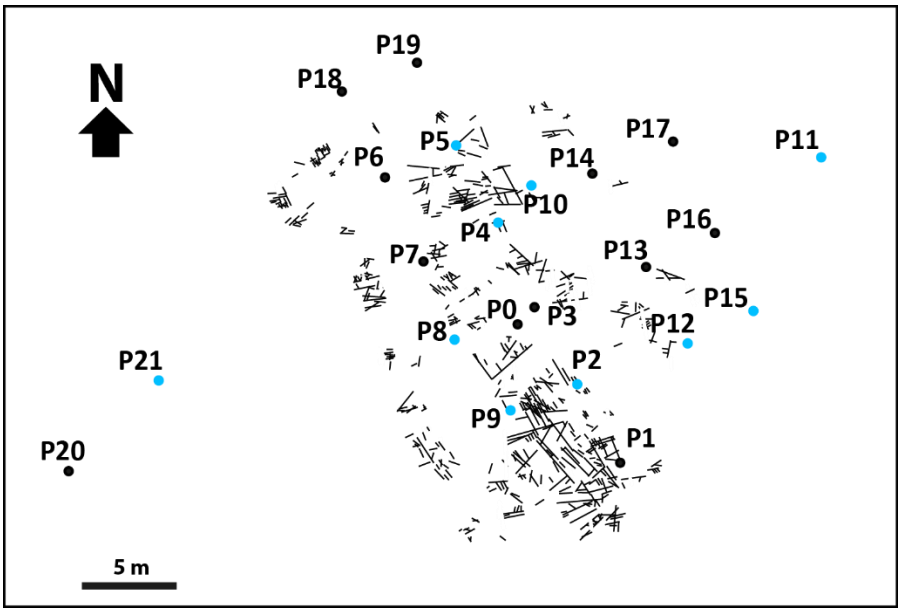

Fig. 2. Well locations and fracture map of the Terrieu site, see Fig. 1. Blue dots indicate boreholes with downhole video data.

1.5 column fitting image

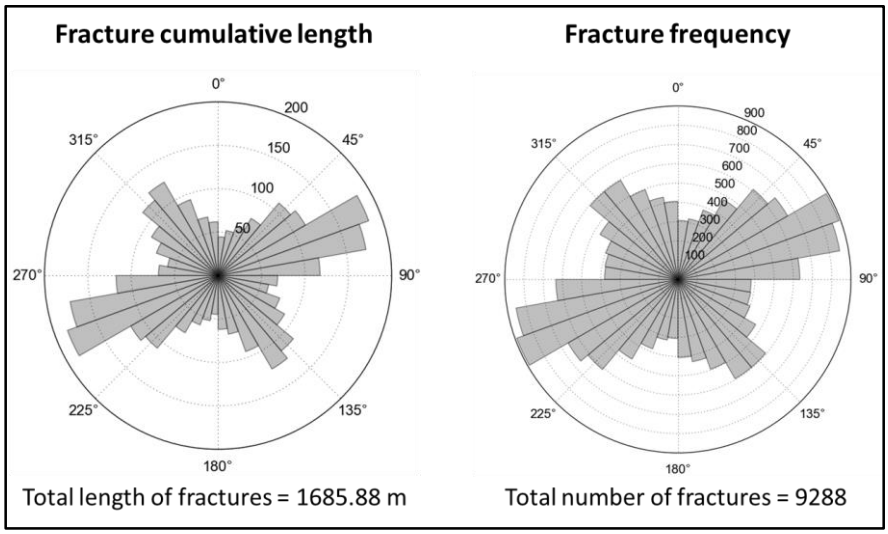

Fig. 3. Rose diagrams derived from fracture analysis on the Terrieu pavement: fracture frequency and cumulative fracture length (in metre).

1.5 column fitting image

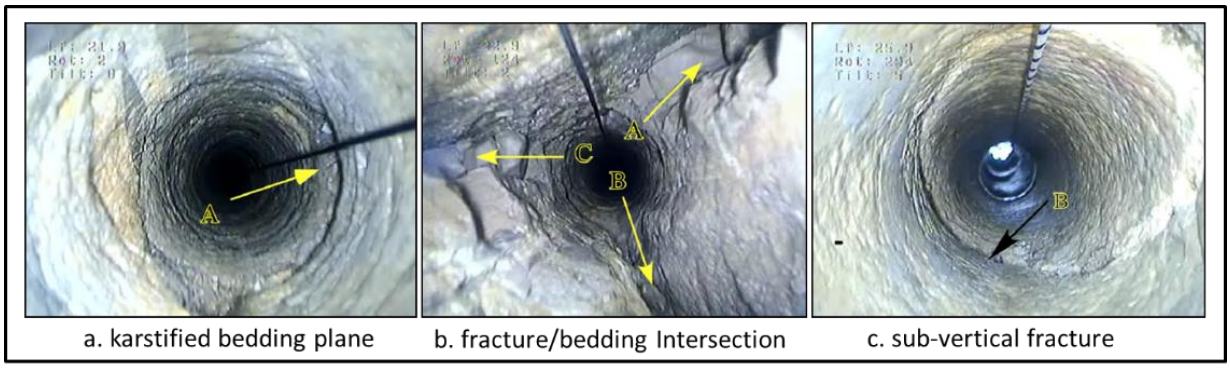

Fig. 4. Examples of the borehole video data. Note that the aperture of the karstic features - up to about 20cm as shown in (b).

2 column fitting image

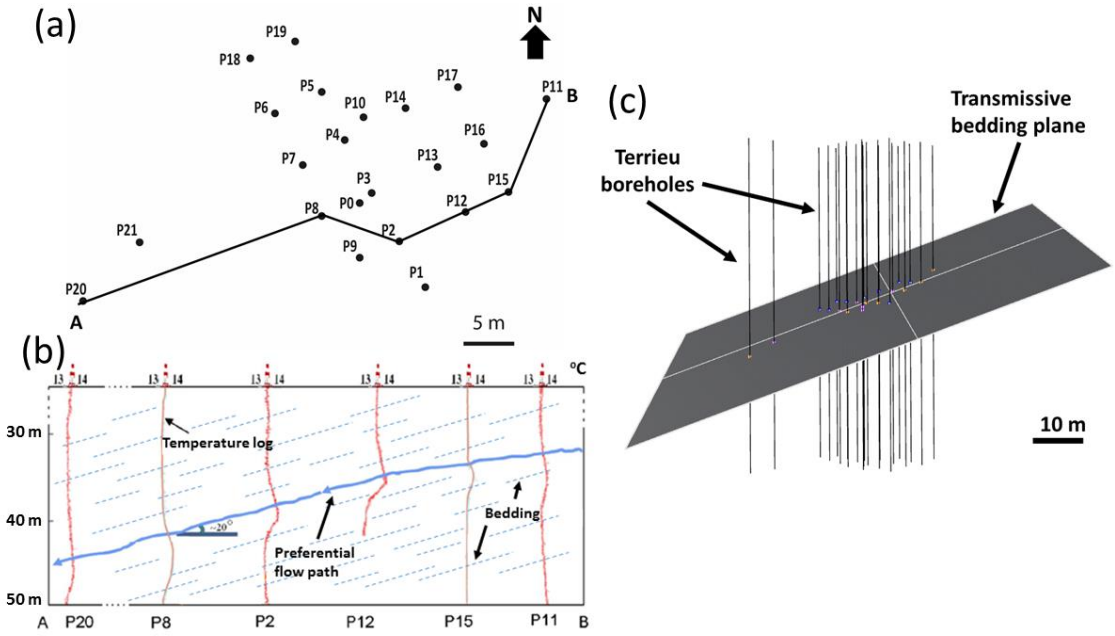

41

42 **Fig. 5**. **(a)** Cross-section trace between well P11 and well P20 at the Terrieu site. **(b)**
43 Temperature log profiles measured in boreholes along the cross-section AB (modified from
44 Jazayeri Noushabadi *et al.* 2011). Note that the deflections in the temperature profiles define
45 the location of the karstified bedding plane, i.e. the preferential flow path. The general dip of
46 the bedding is also indicated by the dashed lines. **(c)** 3D geometry of the karstified bedding
47 plane determined by the correlation of borehole temperature logs and borehole videos. It is
48 found that the groundwater flow on the local scale is strongly constrained within this bedding
49 plane. It has been used as the conceptual model in this work

50 2 column fitting image

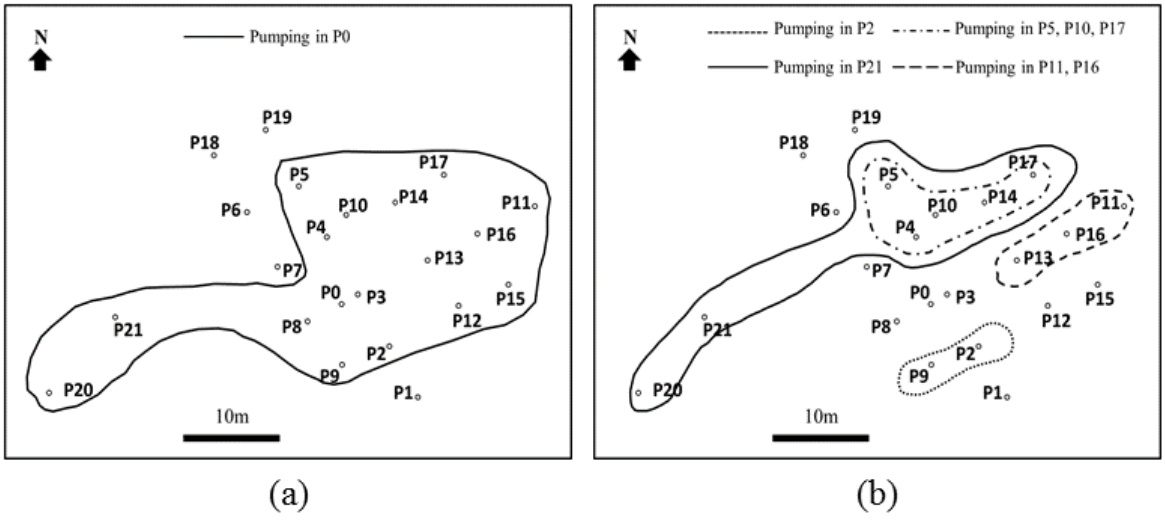

51

52 **Fig. 6**. Connectivity maps inferred from the affected zones during different cross-hole
53 pumping tests (modified after Jazayeri Noushabadi et al., 2011).

54 2 column fitting image

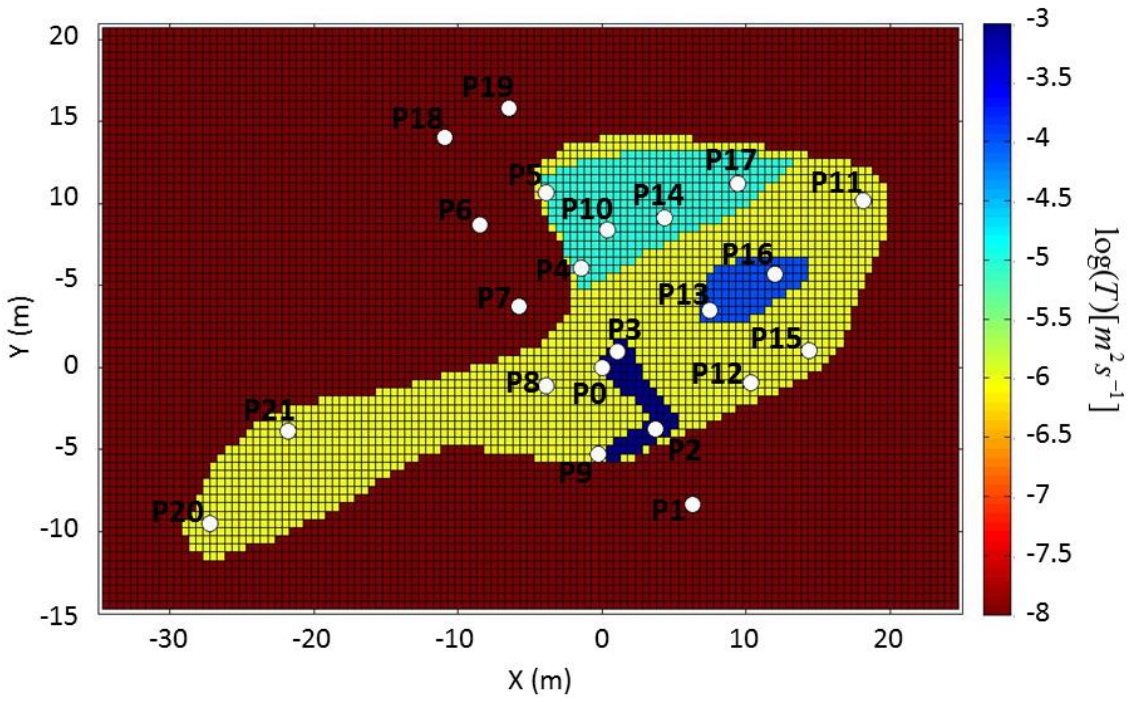

Fig. 7. Inversion model setup with an initial transmissivity field derived from connectivity interpretations based on the cross-hole pumping tests at the Terrieu site.

1.5 column fitting image

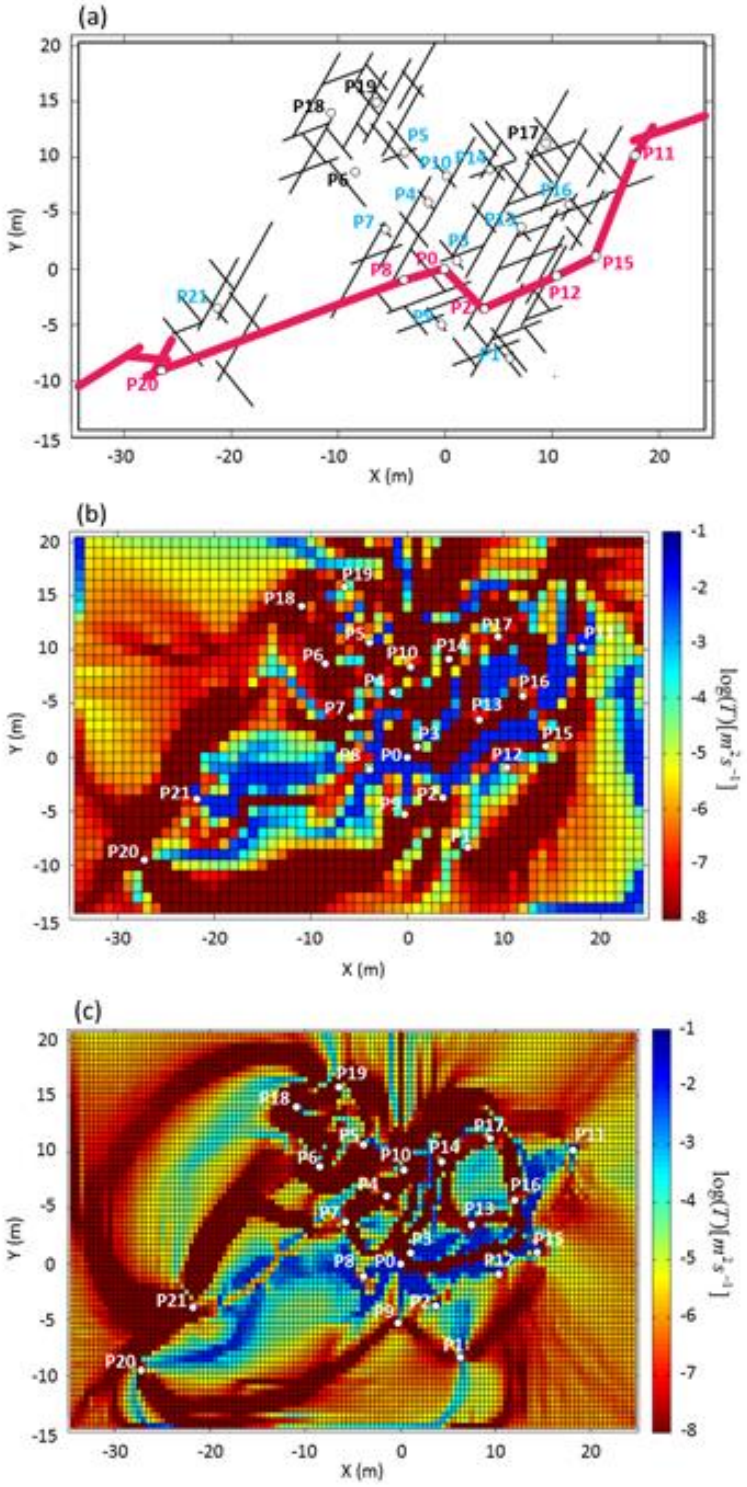

Fig. 8. (a) DFN model used in the synthetic experiment. Three types of borehole-network connectivity were considered in this work are: borehole-karst, borehole-fracture and borehole-matrix (b) Inverted transmissivity field with a grid size of 1m by 1m. (c) Inverted transmissivity field with a grid size of 0.5m by 0.5m.

1.5 column fitting image

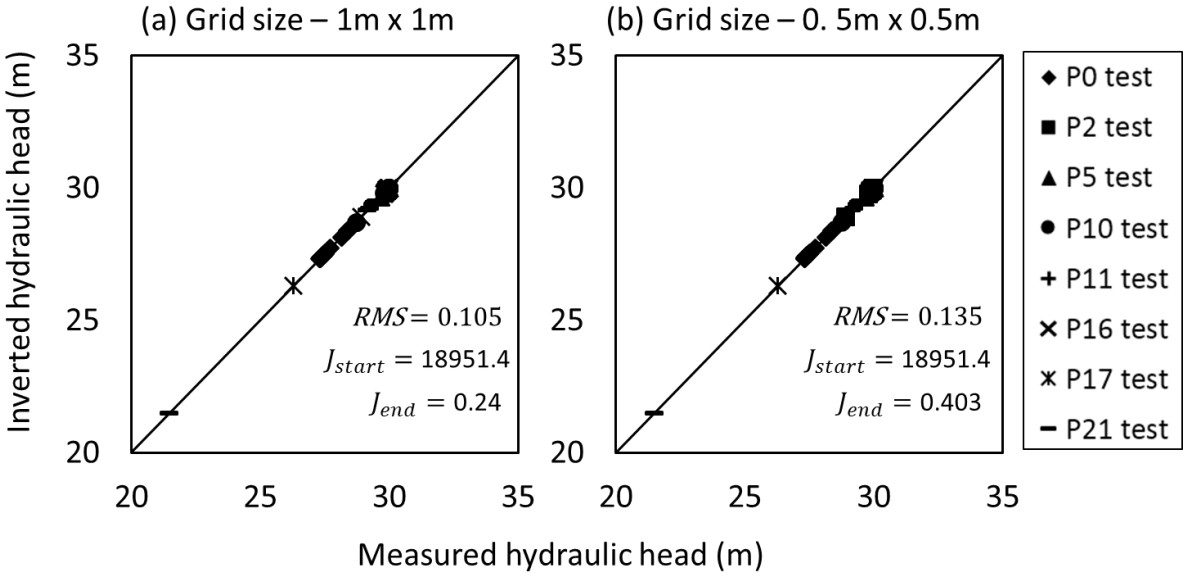

Fig. 9. Correlations of inverted vs. measured hydraulic heads. (a) Results for inversion model with a grid size of 1m by 1m. (b) Results for inversion model with a grid size of 0.5m by 0.5m.

2 column fitting image

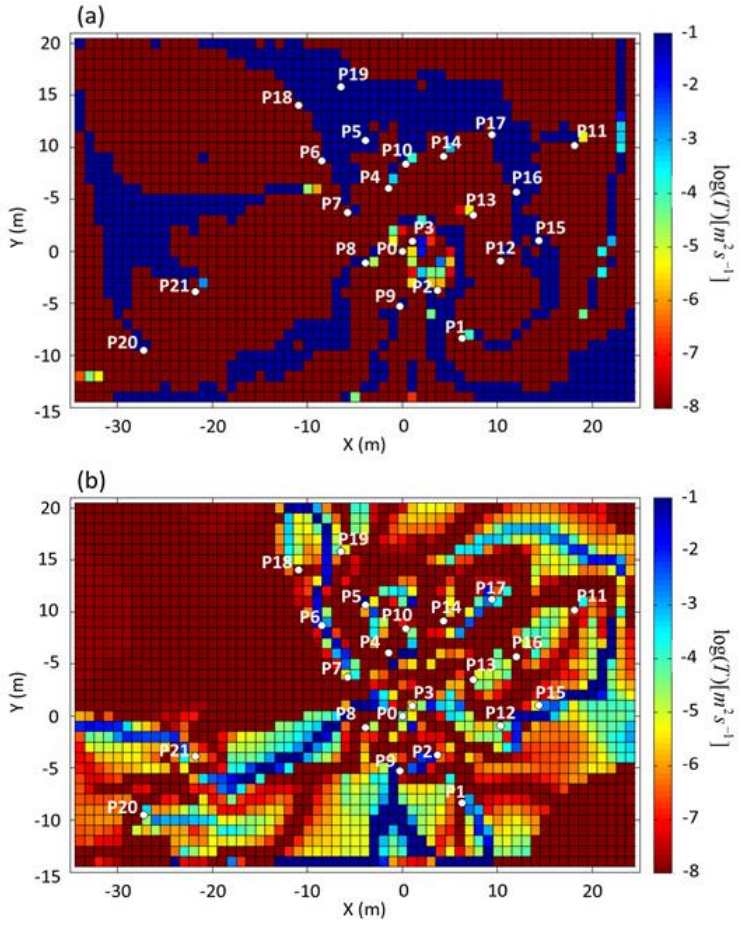

Fig. 10. Comparison of inverted transmissivity fields obtained by using (a) a constant initial transmissivity value ($10^{-4}m^2/s$) for both the local and regional areas as the initial condition in the inversion; (b) an initial transmissivity field, shown in the Fig. 7, as the initial condition in the inversion.

1.5 column fitting image

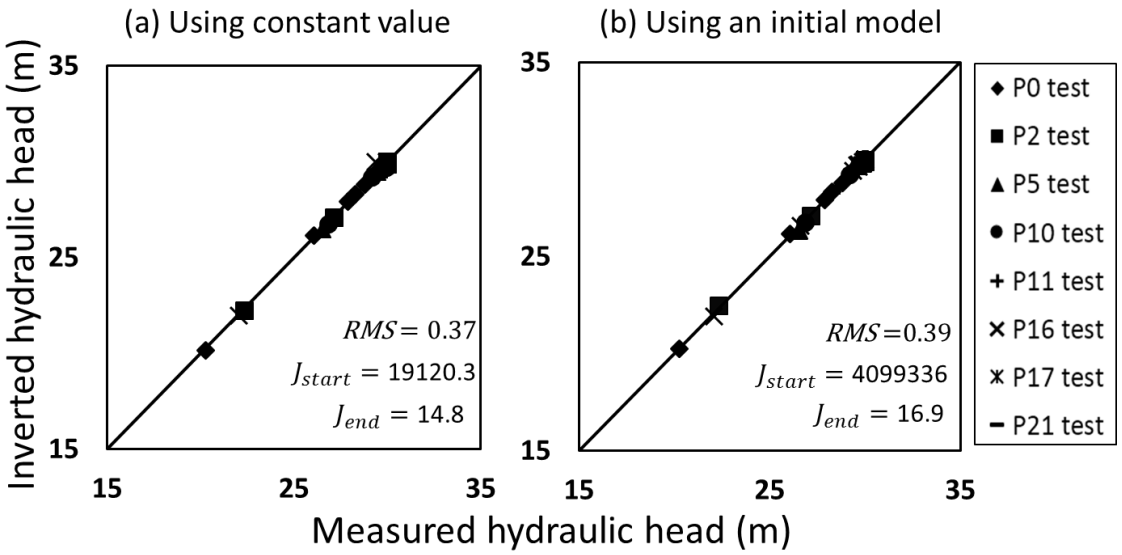

Fig. 11. Scatter plots of observed hydraulic heads versus predicated hydraulic heads: (a) result for using a constant initial transmissivity value ($10^{-4}m^2/s$) for both the local and regional areas as the initial condition in the inversion model; (b) result for using an initial transmissivity field which is shown in the Fig. 7 as the initial condition in the inversion.

2 column fitting image

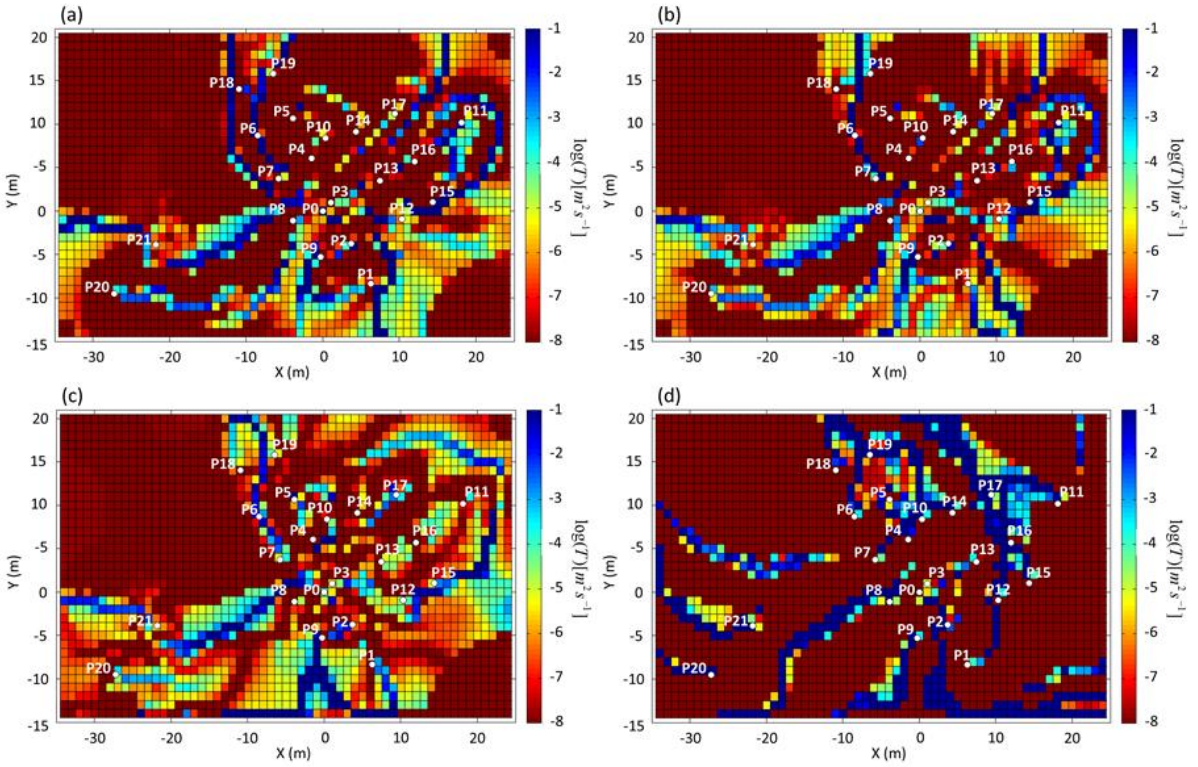

92

93 **Fig. 12**. Comparison of transmissivity fields inverted using different regional transmissivity
94 value. Values of $10^{-2}m^2/s$, $10^{-3}m^2/s$, $10^{-4}m^2/s$, and $10^{-5}m^2/s$ were set in the model (a),
95 (b), (c) and (d) respectively. The range set for the local transmissivities in all the four
96 simulations was $[-8,-1]$ ($\log_{10}$T; m^2s^{-1}).

97 2 column fitting image

98

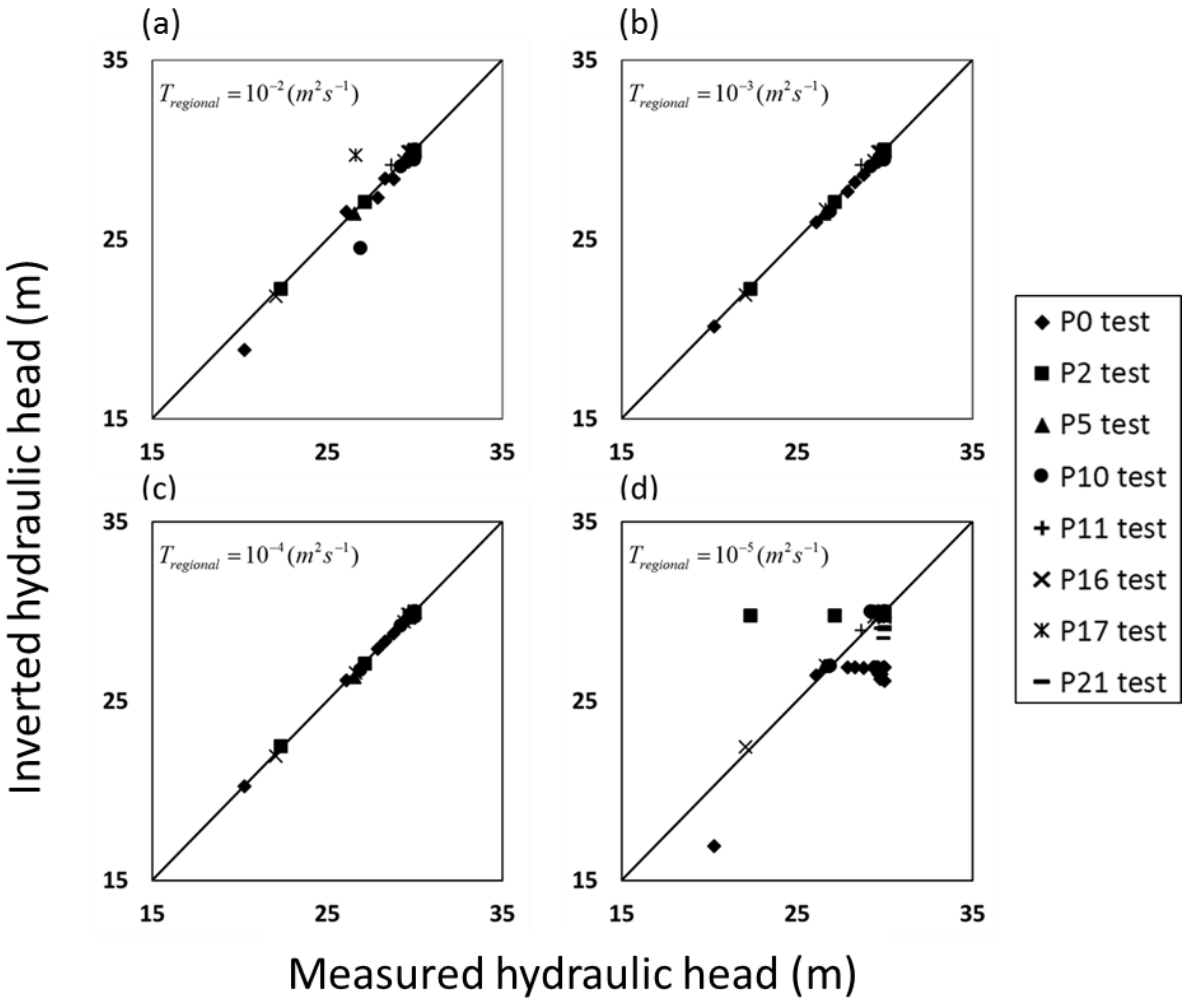

99

100 **Fig. 13**. Scatter plots of observed hydraulic heads versus predicated hydraulic heads for the
101 study of hydraulic transmissivity bounds in the regional buffer area. The inverse models were
102 run by using four different regional transmissivity values. See Table 1 for the inversion
103 performance of the four simulations.

104 2 column fitting image

105

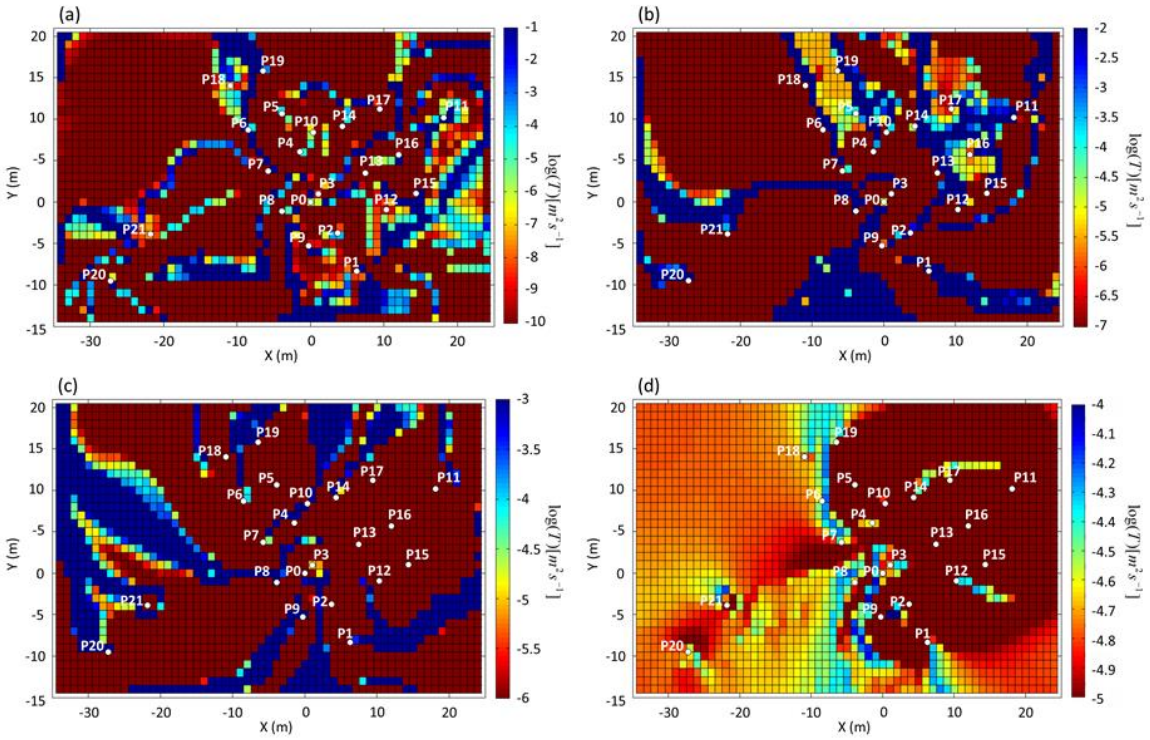

106

107 **Fig. 14**. (a) Transmissivity field inverted using $[10^{-10}, 10^{-1}]$ (m^2s^{-1}) for the local
108 transmissivity range; (b) Transmissivity field inverted using $[10^{-7}, 10^{-2}]$(m^2s^{-1}) for the
109 local transmissivity; (c) Transmissivity field inverted using $[10^{-6}, 10^{-3}]$(m^2s^{-1}) for the local
110 transmissivity; (d) Transmissivity field inverted using $[10^{-5}, 10^{-4}]$(m^2s^{-1}) for the local
111 transmissivity. Note in all the cases, a constant value of $10^{-4}m^2/s$ was considered for
112 transmissivity in the buffer region. See Fig. 10b to compare with the inverse model run with a
113 $[10^{-8}, 10^{-1}]$(m^2s^{-1}) range for local transmissivities.

114 2 column fitting image

115

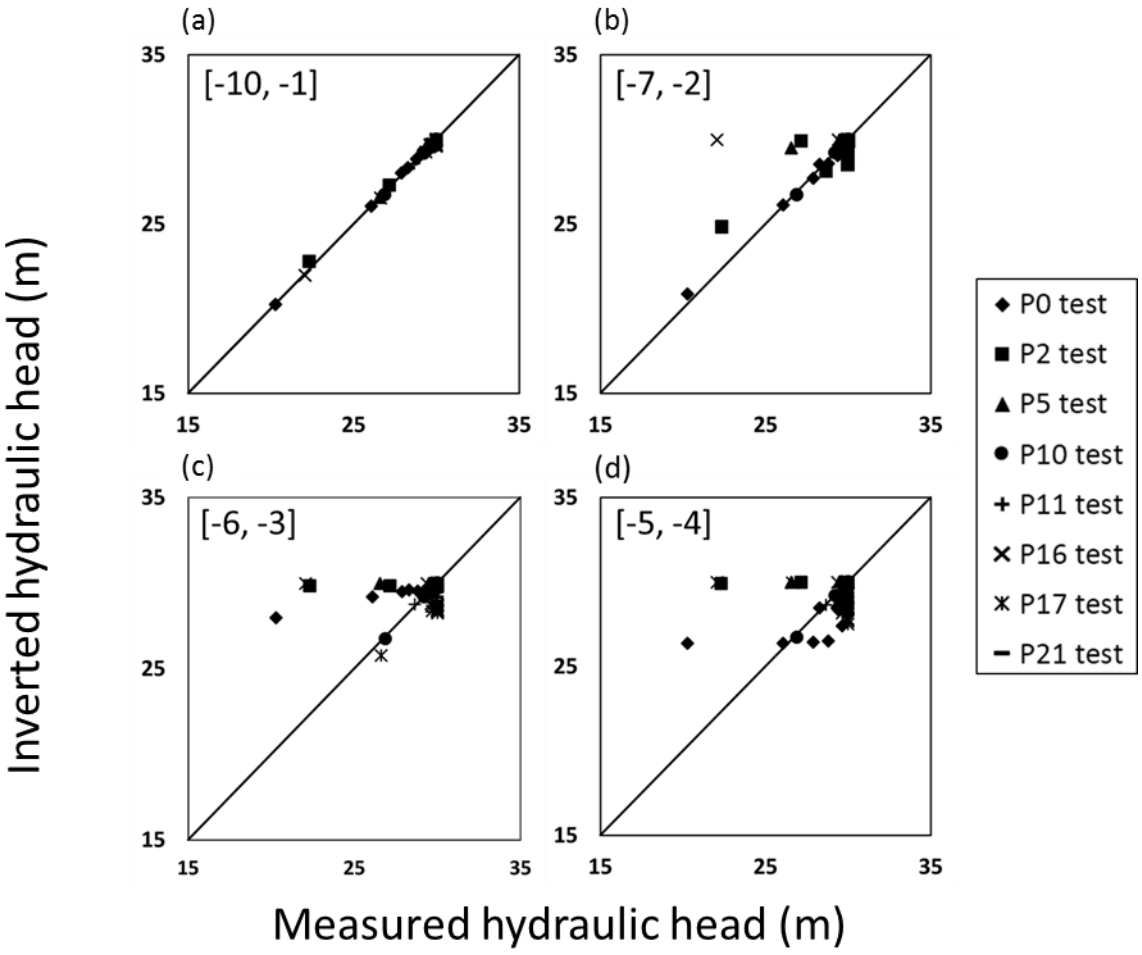

116

117 **Fig. 15**. Scatter plots of observed hydraulic heads versus predicated hydraulic heads for the
118 investigation of bounds for local transmissivities. The inversion models were run with five
119 different ranges for the local spatially varying transmissivities. The regional transmissivity was
120 set to be $10^{-4}(m^2s^{-1})$ for all the five simulation models. See Table 2 for the inversion
121 performance of the five simulations.

122 2 column fitting image

123

124

125

126

127

128

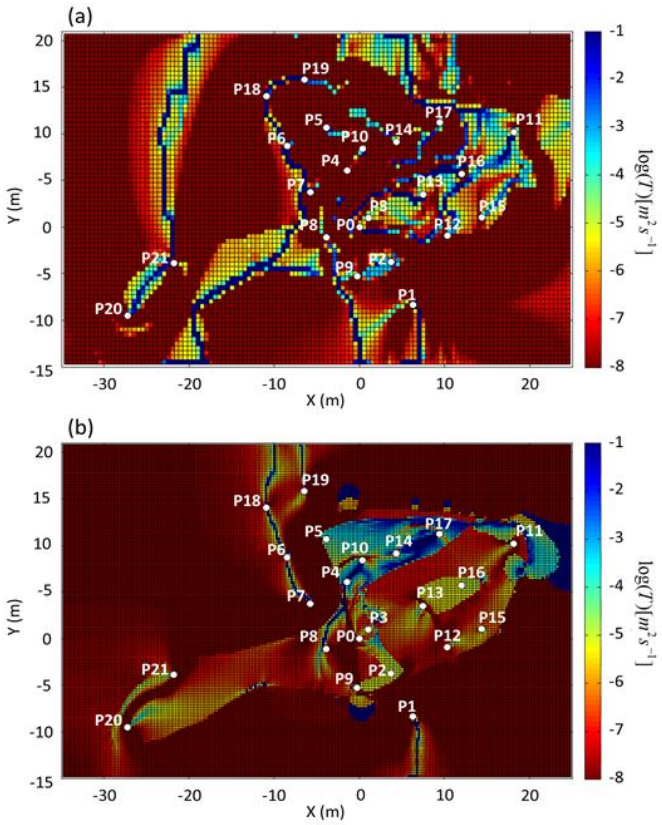

Fig. 16. Comparison of transmissivity fields inverted using different grid sizes. In (a) the grid size is 0.5m by 0.5m; in (b) the grid size is 0.25m by 0.25m. Both models were run by using a constant regional transmissivity value of $10^{-4}(m^2s^{-1})$ and the range for the local transmissivities in these models was set to $[10^{-8}, 10^{-1}](m^2s^{-1})$. In both cases, the *a priori* transmissivity field shown in Fig. 7 was used as the initial condition for the inversion. See also Fig. 10b to compare with inverted transmissivity field obtained by using a grid size of 1m by 1m.

1.5 column fitting image

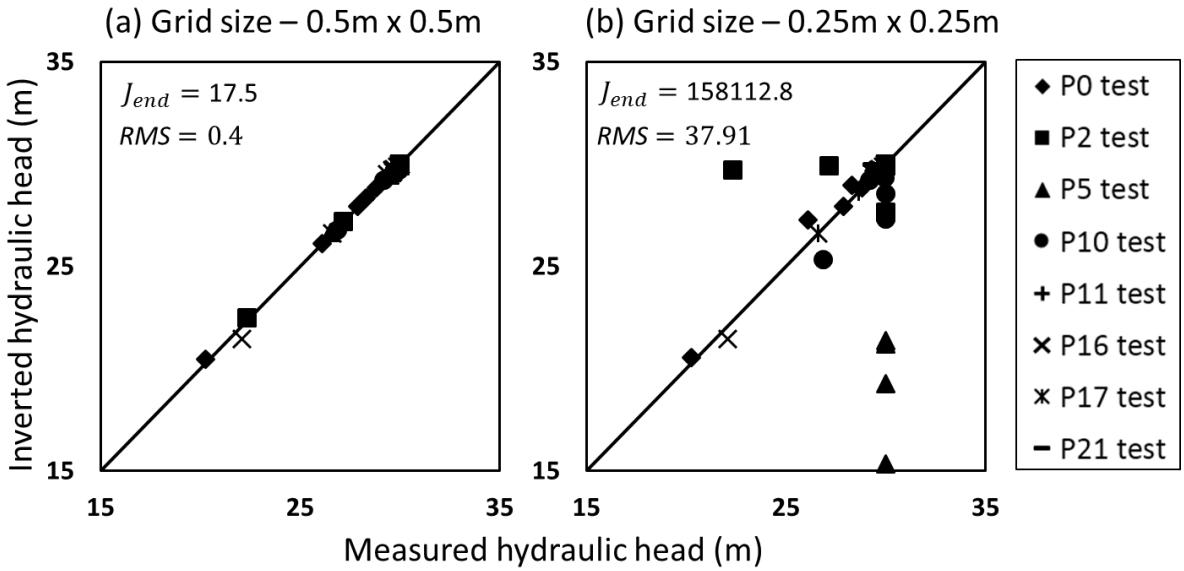

139

140 **Fig. 17**. Scatter plots of observed hydraulic heads versus predicated hydraulic heads: (a) using
141 a 0.5m by 0.5m grid size; (b) using a 0.25m by 0.25m grid size. We note that the inversion
142 model run with the grid size 0.25m by 0.25m did not converge. See text for discussion.

143 2 column fitting image

144